Creep and creep fracture of 2.25Cr-1.6W steels (Grade 23)

M.T. Whittaker and B. Wilshire
Materials Research Centre, School of Engineering, Swansea University, Swansea. SA2 8PP, UK.

Abstract

The creep and creep rupture properties of Grade 23 (2.25Cr-1.6W) steels have been analysed for material produced in pipe (P23) and tube (T23) forms. The similarities and differences in the behaviour patterns observed for the pipe and tube products are then discussed in terms of the dislocation processes governing creep strain accumulation and the various damage phenomena causing the onset of tertiary creep and eventual fracture. Finally, the stresses causing failure of these materials in 100,000h at different temperatures are estimated to provide design data for construction of future power plant.

Keywords: creep; fracture; bainitic steels

1. Introduction

For power and petrochemical plant, large-scale components are usually designed on the basis that creep fracture should not occur under the operating conditions imposed during planned lives of 250,000h. In general, when selecting alloy steels for these applications, decisions are based on the 'allowable creep strengths', normally calculated from the tensile stresses causing failure in 100,000h at the relevant service temperatures [1]. However, creep life measurements for structural steels show considerable batch-to-batch scatter so, in Europe, tests up to 30,000h have often been completed for five melts of each steel grade [2]. Yet, even when using these extensive results, the 100,000h strength estimates depend on the methods adopted to make the calculations [3,4], despite the international activities devoted to the assessment of different data analysis procedures [5]. Moreover, for a series of 9-12% chromium steels developed for ultra super-critical power plant (i.e. Grades 91, 92 and 122), the allowable strengths have been reduced progressively as the test durations have increased well beyond 30,000h towards 100,000h and more [3,4].

In contrast to the problems encountered using traditional parametric, numerical and computational procedures for extrapolation of short-term creep life properties [5], a new methodology appears to allow accurate prediction of 100,000h strengths by considering results with maximum lives up to only about 5000h [6-9]. This new approach, based on normalising the applied stress (σ) through the 0.2% proof stress (σ_{PS}) and/or the ultimate tensile stress (σ_{TS}) at the creep temperatures for each batch of material investigated, has proved successful for a series of ferritic [9], bainitic [8] and martensitic steels [7]. In addition, confidence in this method is improved by interpretation of the property sets in terms of the processes governing creep and creep fracture [6]. Hence, in the present study, this new methodology is adopted for bainitic Grade 23 steels (2.25%Cr-1.6W). Grade 23 steels exhibit creep strengths above those for the bainitic 2.25Cr-1Mo steels (Grade 22) widely used for conventional power plant operating up to 840K, but less than the values for the martensitic 9-12% Cr ranges (Grades 91, 92 and 122) developed for plant service above 875K. Thus, Gr 23 was introduced to reduce the costs of traditional power plant, but the allowable creep strengths remain uncertain [10]. For this reason, the present analysis was conducted using the impressive creep data sheets [10,11] produced at 773 to 923K in air by the National Institute for Materials Science (NIMS), Japan, for both pipe (P23) and tube materials (T23). The substantial differences in the behaviour patterns observed for the pipe and tube products are then discussed in relation to the microstructural changes which occur during creep exposure.

2. Creep of bainitic 2.25Cr-1.6W pipe steel (P23)

For over half a century, the dependencies of the minimum creep rate ($\dot{\varepsilon}_m$) and the creep fracture life (t_f) on stress (σ) and temperature (T) have been described using power law equations of the form

$$M/t_f = \dot{\varepsilon}_m = A\sigma^n \exp(-Q_C / RT) \quad (1)$$

where R = 8.314Jmol^{-1}K^{-1}. From the log $\dot{\varepsilon}_m$ /log σ plots for P23, the stress exponent (n) decreases from around 13 at high stresses at 773K to almost 6 under low stresses at 923K, with the activation energy for creep (Q_c) ranging from about 300 to 535kJmol^{-1} (Fig 1). Similar trends were observed for the log t_f/log σ relationships (Fig. 2). Clearly, the unknown variations in n and Q_c make it impossible to estimate long-term properties by extrapolation of this short term data.

To consider the effects of normalising the applied stress, use was made of the NIMS σ_{PS} and σ_{TS} values [11]. For P23 steel at 773 to 923K, σ_{TS} decreased from 407 to 247 MPa, whereas σ_{PS} declined from 341 to 217 MPa. While σ_{TS} is the highest stress which can be applied at the creep temperature, with $t_f \rightarrow 0$ as $\sigma/\sigma_{TS} \rightarrow 1$, it should be noted that all tests were completed at stresses below σ_{PS}.

Using these results, the power law plots in Figs 1 and 2 were rationalised by normalising σ through σ_{TS} so Eq. (1) can be rewritten as

$$M/t_f = \dot{\varepsilon}_m = = A^* \left(\sigma / \sigma_{TS}\right)^n \exp(-Q_C^* / RT) \quad (2)$$

where A*≠A. Adopting Eq. (2), the data sets at different temperatures are superimposed onto a single curve through an activation energy (Q_c^*) of 230kJmol^{-1} (Figs 3 and 4), where Q_c^* is determined from the temperature dependencies of $\dot{\varepsilon}_m$ and t_f at constant (σ/σ_{TS}), rather than at constant σ as in the determination of Q_c with Eq. (1). However this procedure does not eliminate the decrease from n≅13 to n≅6, so the unknown curvatures of the log $\dot{\varepsilon}_m$ /log (σ/σ_{TS}) and log t_f/log (σ/σ_{TS}) plots in Figs 3 and 4 still does not allow prediction of long-term properties by extrapolation of short-term results for P23 steel.

In contrast, extended extrapolation to provide 100,000h data from tests lasting up to 5000h does appear to be possible using the Wilshire equations [6-9] as

$$\left(\sigma / \sigma_{TS}\right) = \exp\left\{-k_1\left[t_f \exp(-Q_C^* / RT)\right]^u\right\} \quad (3)$$

and

$$\left(\sigma / \sigma_{TS}\right) = \exp\left\{-k_2\left[\dot{\varepsilon}_m \exp(Q_C^* / RT)\right]^v\right\} \quad (4)$$

where the coefficients, k_1 and k_2 as well as u and v, are easily determined from plots of ln[$\dot{\varepsilon}_m$ .exp (Q_c^*/RT)] and ln[t_f exp (-Q_c^*/RT)] against ln [-ln (σ/σ_{TS})]. These plots, shown as Figs. 5 and 6, indicate that changes in slope occur with P23 as the applied stress falls below 0.85σ_{PS}, particularly at 773K. This coincides with a change from k_1 = 31 and u = 0.20 at high stresses to k_1 = 9.5 and u = 0.15 at low stresses with Eq. (3), as determined from the results of tests with t_f < 5000h. Similarly, a fall from k_2 = 15 and v = -0.20 at high stresses to k_2 = 6.1 and v = -0.15 at low stresses occurs with Eq. (4). Inserting

these values into Eqs. (3) and (4) then produces the reasonable descriptions of the property sets in Figs. 1 and 2. In this way, the actual creep lives are longer and the creep rates are slower when $\sigma < 0.85\sigma_{PS}$ than would be expected by linear extrapolation of the results when $\sigma > 0.85\sigma_{PS}$.

3. Creep of bainitic 2-25Cr – 1.6W tube steel (T23)

The T23 material displayed mechanical properties, as well as creep and creep fracture behaviour, significantly different to the P23 product, even though their compositions, processing and thermal histories were comparable [11]. Specifically, the pipe samples had a hardness of HV182 compared with HV207 for the tube, consistent with the T23 having a finer austenitic grain size number. Even so, adopting Eq. (1), the log $\dot{\varepsilon}_m$ /log σ and log t_f/log σ plots for T23 (Figs 7 and 8), appeared similar to those for P23 (Figs. 1 and 2). Thus, a decrease from $n \cong 14$ to $n \cong 6$ was accompanied by a substantial increase from $Q_c \cong 300$ to $Q_c \cong 500 kJmol^{-1}$ with decreasing stress and increasing temperature for the T23 steel.

As with the P23 samples, the plots in Figs 7 and 8 could be rationalised through Eq. (2), with $Q_c^* \cong 230 kJmol^{-1}$, but the unknown reduction in n value with increasing test duration and temperature again makes extended extrapolation unreliable. However, utilizing a fall in σ_{TS} from 455MPa to 280MPa on increasing the test temperature from 773 to 923K, a difference in behaviour pattern was noted between the results for P23 (Figs 3 and 4) and for T23 (Figs. 9 and 10). Essentially, with P23, the creep life decreased gradually with increasing time and temperature, whereas a sharper fall in life occurs as the test duration increases at 873K and above with the T23 material.

Even greater differences between the data sets for P23 and T23 were evident using Eqs. (3) and (4), with the $\ln[\dot{\varepsilon}_m . \exp(Q_c^*/RT)]$ and $\ln[t_f \exp(-Q_c^*/RT)]$ against $\ln[-\ln(\sigma/\sigma_{TS})]$ relationships presented for T23 in Figs 11 and 12. Essentially, the results for T23 are best described by three intersecting straight lines, with the k_1, k_2, u and v values for each section derived from data with $t_f < 5000h$ included in Table I. Incorporating the results in Table I into Eqs. (3) and (4) accurately describes the long-term data (Figs. 7 and 8), but it then becomes necessary to explain the behavioural differences recorded for P23 and T23.

As with P23, on decreasing the applied stress and increasing the creep temperature, a change in k_1 and u in Eq. (3), as well as in k_2 and v with Eq. (4), at $\sigma < 0.85\sigma_{PS}$ with T23 signifies that the creep lives are longer and the creep rates are slower at lower stress than would be predicted by linear extrapolation of results when $\sigma > 0.85\sigma_{PS}$. In contrast, with T23, further changes in the values of these coefficients means that, in long-term tests at 873K and above, the creep lives are much shorter and the creep rates substantially faster than would be expected on extrapolation of the intermediate stress/temperature data.

4. Interrelation of creep and creep fracture

The parameter $M(=\dot{\varepsilon}_m.t_f)$ in Eqs. (1) and (2) is not a constant, but varies with stress and temperature (Fig. 13). For P23, $\dot{\varepsilon}_m.t_f$ increases from around 0.02 to a maximum of 0.06 as the stress is decreased towards 150MPa, then falls to about 0.03 after long test times at 873K and above. A similar trend occurs with T23, although the $\dot{\varepsilon}_m.t_f$ values are significantly smaller over the entire range of test conditions studied (Fig.13).

Interestingly, the data trends for $\dot{\varepsilon}_m.t_f$ in Fig.13 are mirrored reasonably by the stress and temperature dependencies of the total strains to failure or creep ductility (ε_f) in Fig.14. For P23, ε_f again increases from around 0.2 to a maximum of 0.45 as the stress falls to just below 150MPa, with a reduction to $\varepsilon_f \cong$ 0.3 to 0.4 in lower stress tests at the higher temperatures (Fig.14). Yet, with T23, while the ε_f values were again lower than those for P23 at all stress/temperature combinations, markedly different behaviour patterns were found under low stresses at higher temperatures. Thus, at 773 and 823K with T23, ε_f again increased slightly from around 0.20 to 0.30 as the stress was reduced to 150MPa, but with a serious fall to $\varepsilon_f < 0.1$ as the stress was decreased towards 100MPa at 873K and above. Moreover, it seems that ε_f then increases towards 0.2 as the stress is further reduced at 923K.

The creep ductility/stress relationships in Fig.14 are reinforced by the measurements recorded for the reduction in area at fracture (RoA) in Fig.15. Thus, with P23, RoA $\cong$ 0.80 at all stress/ temperature conditions. However, with T23, while RoA $\cong$ 0.80 at stresses down to around 150MPa, the reduction in area falls to near zero in the long-term tests at 873K, but is followed by a further rise towards RoA $\cong$ 0.6 in long duration tests at 898K and 923K (Fig.15). Clearly then, the failure modes differ for P23 and T23 under different stress/temperature conditions.

Although the product, $\dot{\varepsilon}_m.t_f$, varies with stress and temperature (Fig.13), the approximately inverse dependence of t_f on $\dot{\varepsilon}_m$ means that the creep life is determined by the overall creep rate, i.e. fracture is strain controlled. For this reason, the processes determining the differences in the creep behaviour of P23 and T23 are discussed, (e.g. Figs. 5, 6, 11 and 12), before considering the influences of variations in fracture mode.

5. Creep Deformation Processes

With both P23 and T23, changes in the coefficients in Eqs. (3) and (4) occur when $\sigma < 0.85\sigma_{PS}$, such that the creep lives are longer and the creep rates are slower at lower stresses. As previously found for 1Cr-0.5Mo ferritic steels [9]., this takes place when $\sigma < \sigma_Y$, where σ_Y is the yield stress determined in high-strain-rate ($10^{-3}s^{-1}$) tensile tests carried out at the creep temperatures for each batch of material investigated. For P23 and T23, it seems reasonable that $\sigma_Y \cong 0.85\sigma_{PS}$. Thus, when $\sigma > \sigma_Y$, dislocations multiply rapidly during the initial strain on loading at the creep temperature, giving high creep rates and shorter creep lives. In contrast, when $\sigma < \sigma_Y$, creep must occur not by the generation of new dislocations but by the movement of the dislocations pre-existing in the as-received bainitic microstructure, giving slower creep rates and correspondingly longer creep lives.

At stresses below $0.85\sigma_{PS}$, k_1 and u, as well as k_2 and v, are constant for P23 at all other stress/temperature combinations. However, with T23, further changes in these parameters are found as the test durations increase at 873K and above. With both products, the creep process degrades the initial bainitic microstructures, such that the original lath-like structure entirely disappears in long-term tests at the higher creep temperatures with T23. These changes are replicated by hardness measurements [10] on samples crept for different times at different temperatures (Fig. 16). Specifically, the gradual fall in hardness with P23 contrasts with a much

slower hardness reduction with T23, until a sharp fall in hardness occurs with T23 in long-term tests at 898 and 923K.

The hardness of the P23 (HV 182) is lower than that of T23 (HV 207) in the as-received state, indicating that P23 is more heavily tempered. As a result, further tempering during creep of the P23 is slow. In contrast, with the T23, the slow initial fall in hardness suggests only a gradual degradation of the initial bainitic microstructure, until a sudden hardness fall is caused as the lath-like structure disappears after long creep times at 873K and above. Thus, the creep rate increases sharply, leading to a corresponding fall in creep life, as the bainitic microstructure of the T23 degrades rapidly with increasing test duration and temperature.

6. Tertiary creep and Fracture Processes

Under high temperature creep conditions, most materials display normal creep curves, i.e. after the initial strain on loading, the creep strain (ε) increases with time (t) at a creep rate ($\dot{\varepsilon} = d\varepsilon / dt$) which decays during the primary stage, reaching a secondary or minimum rate before increasing during the tertiary stage which leads to fracture. Even so, plotting $\dot{\varepsilon}$ against t demonstrates that instead of a secondary or steady state stage, only a minimum rate ($\dot{\varepsilon}_m$) is reached when the decaying primary rate is offset by the tertiary acceleration. Rather than seeking to identify 'steady state' creep mechanisms, attention should therefore be focussed on the deformation processes governing strain accumulation and the damage phenomena causing the tertiary acceleration and eventual fracture.

Under all conditions studied for P23 and T23, creep occurs by the movement of dislocations, irrespective of whether dislocations are or are not generated during the initial specimen extension on loading. Hence, the fact that $Q_C^* \cong 230 kJmol^{-1}$ suggests that this value represents the activation energy for diffusion-controlled dislocation movement in the bainitic microstructure. Yet, while the dominant dislocation processes controlling creep are the same as the bainitic microstructures degrade, the phenomena causing the onset of tertiary creep and eventual fracture differ, depending on the test conditions imposed with P23 and T23.

A measure of the processes occurring during the onset of the tertiary creep stage is [12,13] the creep damage tolerance parameter (λ) where [14]

$$\lambda = \left(\varepsilon_f - \varepsilon_p\right) / \dot{\varepsilon}_m t_f \approx \varepsilon_f / \dot{\varepsilon}_m t_f \qquad (5)$$

where ε_p is the primary strain, which is sufficiently low to suggest that (ε_f- ε_p) can be approximated by ε_f. In this way, when $\lambda \cong 1$ to 2, tertiary begins as a consequence of cavitation, whereas tertiary starts because of either necking or microstructural instability when λ>2 [13].

With P23, RoA $\cong$ 0.8 (Fig.15) with RoA > ε_f, so that λ>2 suggests that neck formation at 723K and microstructural instability at 823K and above cause tertiary creep and transgranular fracture. However, with T23, the differences in the results recorded for the stress and temperature

dependencies of $\dot{\varepsilon}_m.t_f$, ε_f and RoA (Figs 13, 14 and 15) indicate that the damage processes differ significantly from those for P23.

As with P23, the data for T23 suggests that tertiary begins by necking at 773K and by microstructural instability at the higher temperatures, leading to transgranular fracture. Yet, the rapid fall in ε_f and RoA when $\sigma <$ 150MPa indicates a transition in failure mode to creep cavitation with T23. Even so, cavity development is then limited by grain boundary migration in the degraded T23 microstructure at low stresses at 873K and above. This then accounts for the ε_f and RoA behaviour shown in Figs. 14 and 15. However, these phenomena occur during the tertiary stage without affecting $\dot{\varepsilon}_m$, so the stress and temperature dependencies of $\dot{\varepsilon}_m.t_f$ in Fig. 13 for P23 and T23 are essentially similar.

7. Long –Term Design Data for Grade 23 Steels

Using the k_1 and u values, as well as the k_2 and v results (Table I), incorporation of these figures into Eqs. (3) and (4) give the stress/ log [$\dot{\varepsilon}_m$ .exp (Q_c^* /RT)] and stress/log [t_f exp (-Q_c^* /RT)] plots shown in Figures 17 and 18 [10,11]. Moreover, the sigmoidal shape of these curves are fully compatible with the idea that $\dot{\varepsilon}_m \rightarrow \infty$ and $t_f \rightarrow 0$ as $\sigma/\sigma_{TS} \rightarrow 1$, whereas $\dot{\varepsilon}_m \rightarrow 0$ and $t_f \rightarrow \infty$ as $\sigma/\sigma_{TS} \rightarrow 0$.

Even so, the fact that two breaks occur with T23 (Figs. 11 and 12) compared with one for P23 (Figs. 5 and 6) causes problems. Especially when considering data from tests with $t_f <$ 5000h, there are only a limited number of results available for calculating the values of the coefficients in Eqs. (3) and (4) over certain stress ranges. Hence, the $\dot{\varepsilon}_m$ and t_f values predicted from Eqs. (3) and (4) for T23 do not always match the measured data, as occurs with the $\dot{\varepsilon}_m$ values at 773K (Fig. 7).

Despite this problem, using Eqs. (3) and (4), the stresses causing failure of P23 and T23 in 100,000h at each creep temperature are listed in Table II. Clearly, at temperatures of 873K and above, the 100,000h strength estimates are very much lower for the tube than for the pipe material. Additionally, even the figures for the pipe material in Table II are significantly below earlier estimates [15], namely, 114MPa at 848K, 90.2MPa at 873K and 66MPa at 898K. Obviously, the estimates in Table II were made using data from small diameter specimens so, compared with large thickness pipe and tube in service, oxidation can markedly reduce the 'apparent' strengths at high temperatures [15]. However, the present analyses were made using results with creep lives less than 5000h, when oxidation should be limited. Moreover, the oxidation rates would appear to be similar for the pipe and tube products, which have comparable compositions [10,11]. On this basis, it appears that the very low 100,000h strengths predicted in Table II for T23 are attributable to degradation of the bainitic microstructure with increasing creep exposure at 850K and above. In turn, these low values suggest that Grade 23 steels, particularly the tube products, cannot be used for construction of power plant operating at temperatures approaching 850K.

8. Conclusions

The creep and creep fracture behaviour of Grade 23 steels, normally characterized by power law descriptions of the minimum creep rates and rupture lives, are rationalized by normalizing the applied stress through the proof stress (σ_{PS}) and/or the ultimate tensile stress (σ_{TS}) determined from

high-strain-rate tensile tests carried out at the creep temperatures. Using new relationships, termed the Wilshire equations, these rationalization procedures allow the data sets for Gr 23 steels in pipe (P23) and tube (T23) forms to be discussed in terms of the dislocation processes controlling creep strain accumulation and the different damage phenomena causing tertiary creep and eventual failure as the as-received bainitic microstructures degrade with increasing test duration and temperature. Moreover, these new relationships also enable long-term data to be predicted by extrapolation of short-term results, suggesting that Gr 23 steels should not be used at temperatures approaching or exceeding 850K for future power plant construction.

References

[1] ASME Boiler & Pressure Vessel Code, Sec. II, Part D, Appendix I, ASME 2004.

[2] J. Hald, *Mater. High Temp* **21** (2004) 41-46.

[3] W. Bendick, J. Gabrel, In: I.A. Shibli, S.R. Holdsworth, G. Merckling editors Proc ECCC Int. Conf. on Creep and Fracture of high temperature components – design and life assessment issues. London: DEStech Publ; (2005) 406-418.

[4] L. Cipolla, J. Gabrel. In: Proc. First Int. Conf. on Super high strength steels. Rome: AIM; CD-Rom, (2005).

[5] S.R. Holdsworth et al, In: I.A. Shibli, S.R. Holdsworth, G. Merckling . editors Proc ECCC Int. Conf. on Creep and Fracture of high temperature components – design and life assessment issues. London: DEStech Publ; (2005)380-393.

[6] B. Wilshire, A.J. Battenbough, *Mater. Sci. Eng A.* **443A** (2007), 156-166.

[7] B. Wilshire, P.J. Scharning, *Int. Mater. Rev.* **53** (2008): 91-104.

[8] B. Wilshire, P.J. Scharning, *Mater. Sci. Tech.* **24**, (2008) 1-9.

[9] B. Wilshire, P.J. Scharning, *Int. J. Press. Vessels and Piping* **85** (2008) 739-743.

[10] K. Sawada et al, In: I.A. Shibli, S.R. Holdsworth editors. Proc. Second ECCC conference on Creep and Fracture in High temperature components – design and life assessment issues. Zurich: DEStech Publ; 2009. 79-92.

[11] NIMS Creep Data Sheet No.54. 2008.

[12] M.F. Ashby, B.F. Dyson In: Valluri SR. editor. Advances in fracture research, Oxford, Pergamon Press, 1984, 3-30.

[13] B. Wilshire, H. Burt, In: I.A. Shibli, S.R. Holdsworth, G. Merckling . editors. Proc: ECCC Int. Conf. on creep and fracture of engineering components – design and life assessment issues. London: DEStech Publ; 2005, 191-200.

[14] F.A. Leckie , D.R. Hayhurst, *Acta Mater.* **25** (1977) 1059-1070.

[15] M. Ingarashi, M. Yoshizawa, H. Matsuo, O. Miyahara, A. Iseda, *Mater. Sci. Eng. A*. **510-511A** **(**2009) 104-109.

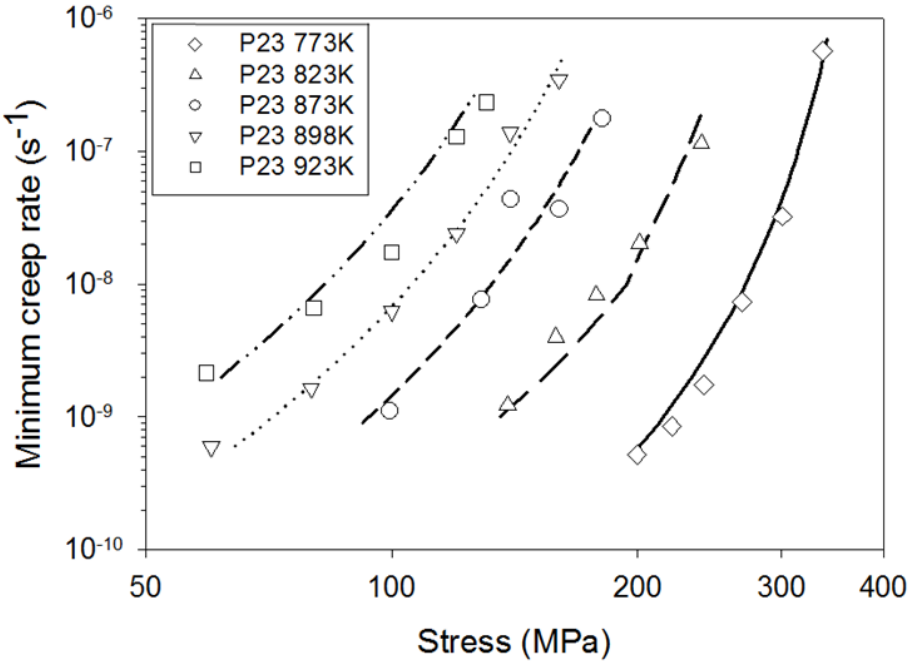

Fig 1. The stress dependence of the minimum creep rate at 773 to 923K for 2.25Cr-1.6W steel pipe (P23). The lines are drawn after analysing the results according to Eq. (4).

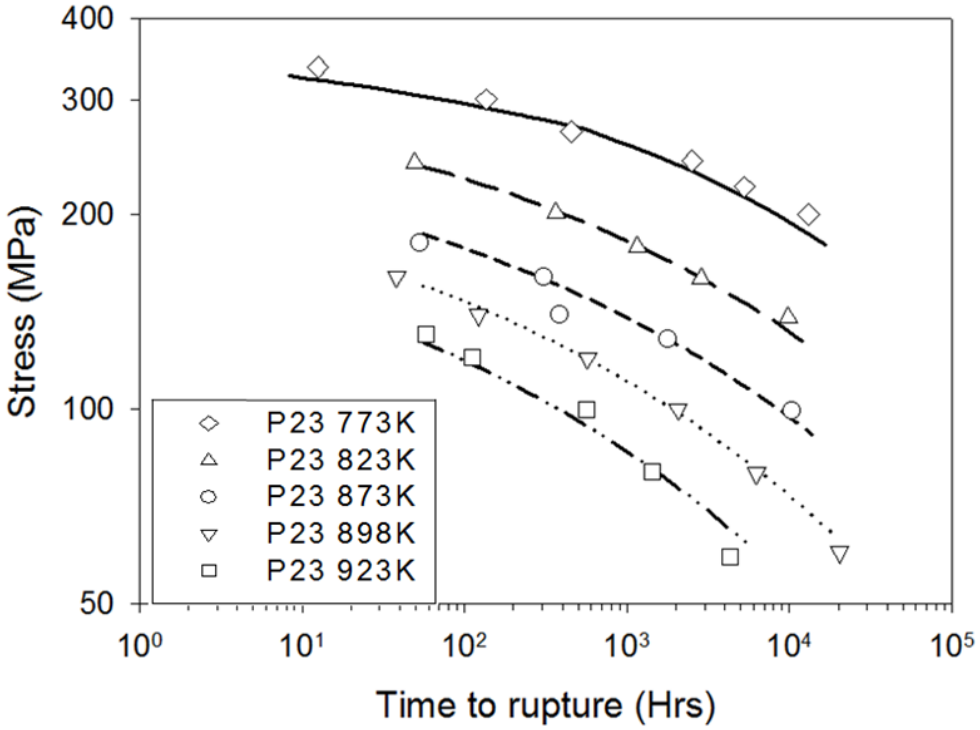

Fig 2. The stress dependence of the creep life at 773 to 923K for 2.25Cr-1.6W steel pipe (P23). The lines are drawn after analysing the results according to Eq. (3).

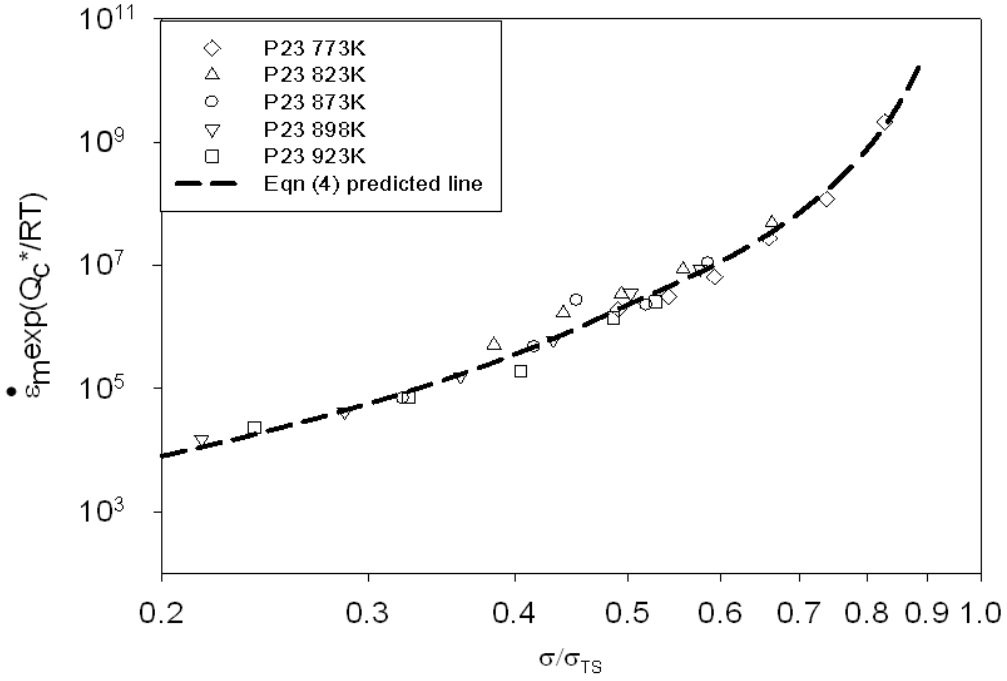

Fig 3. The dependence of log($\dot{\varepsilon}_m$ .exp 230,000/RT) on log (σ/σ_{TS}) at 773 to 923K for 2.25Cr-1.6W steel pipe (P23) using Eq. (2).

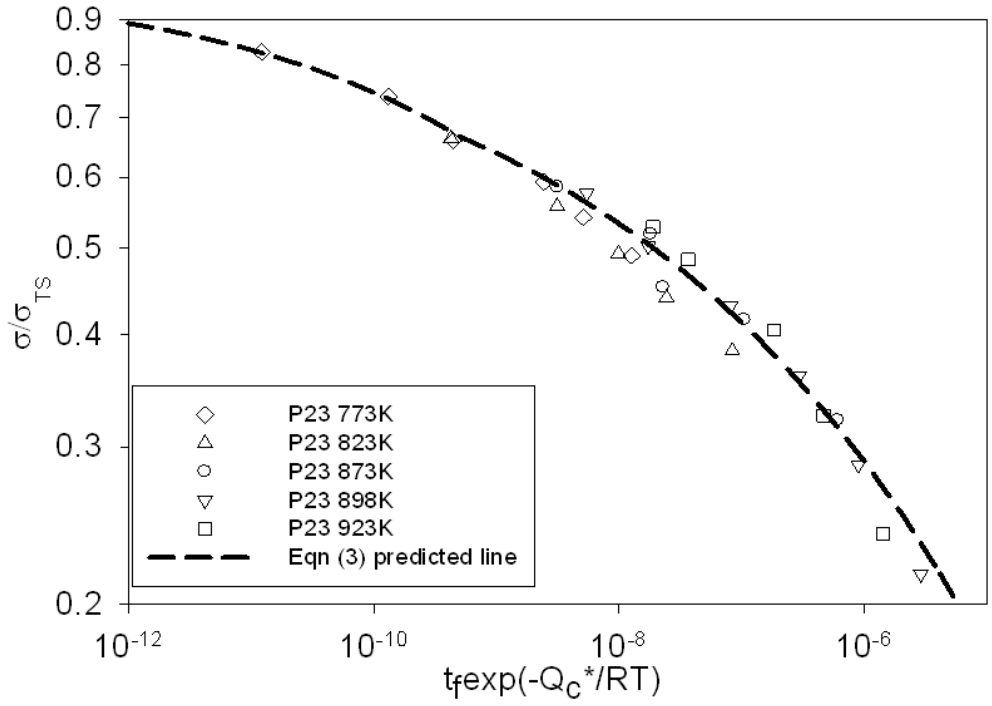

Fig 4. The dependence of log(t_f.exp -230,000/RT) on log (σ/σ_{TS}) at 773 to 923K for 2.25Cr-1.6W steel pipe (P23) using Eq. (2).

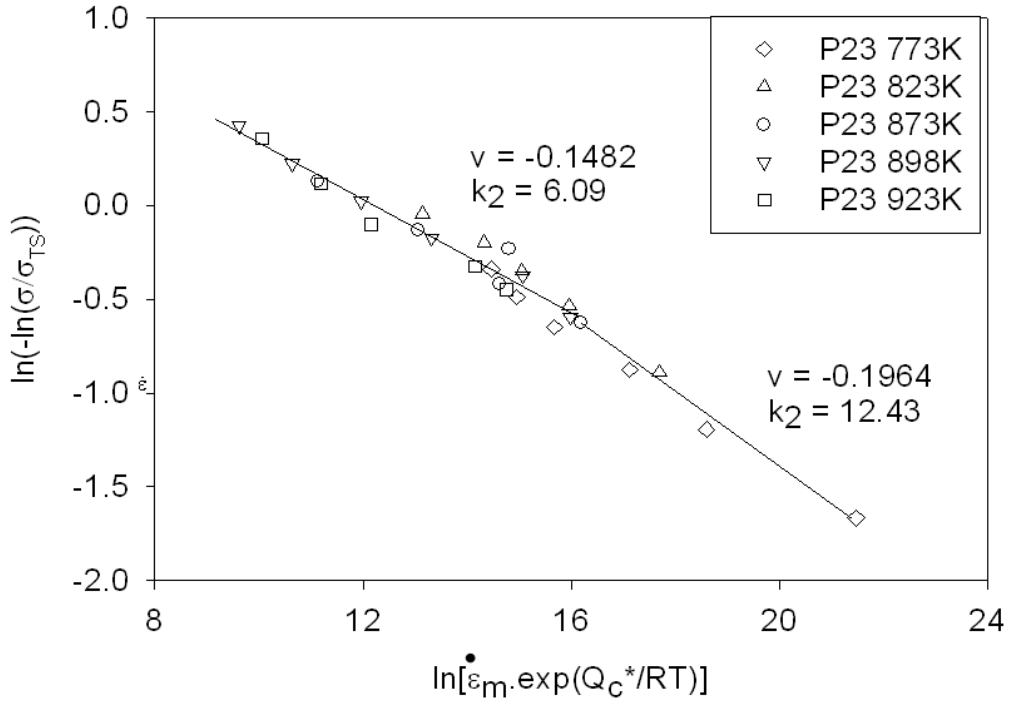

Fig 5. The dependence of $\ln(\dot{\varepsilon}_m \cdot \exp 230{,}000/RT)$ on $\ln(-\ln(\sigma/\sigma_{TS}))$ at 773 to 923K for 2.25Cr-1.6W steel pipe (P23) using Eq. (4).

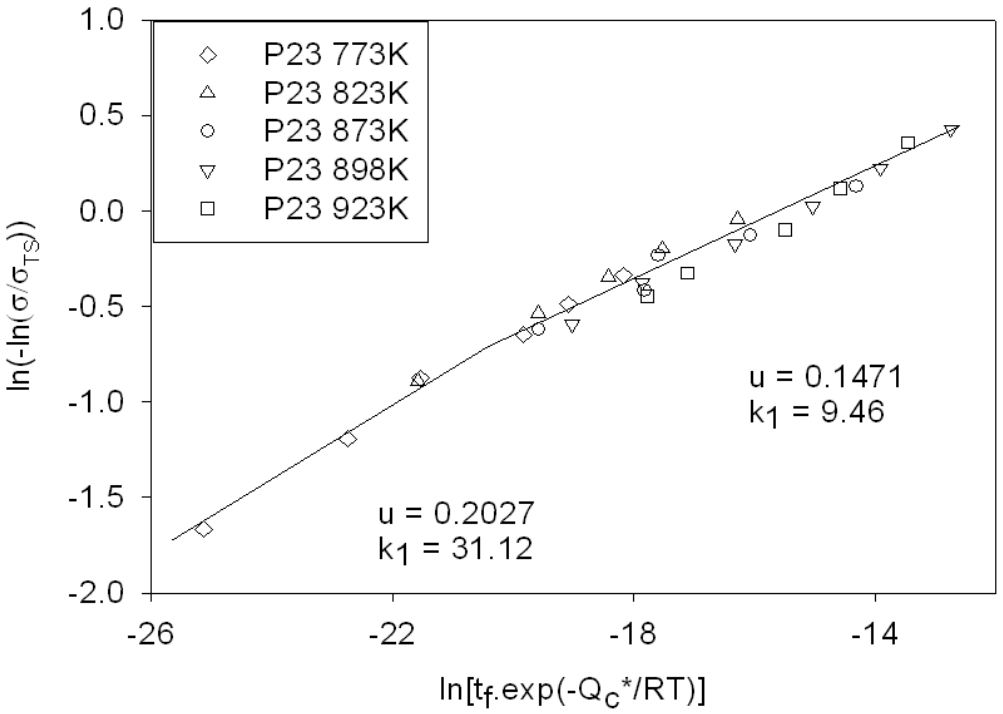

Fig 6. The dependence of $\ln(t_f \cdot \exp -230{,}000/RT)$ on $\ln(-\ln(\sigma/\sigma_{TS}))$ at 773 to 923K for 2.25Cr-1.6W steel pipe (P23) using Eq. (3).

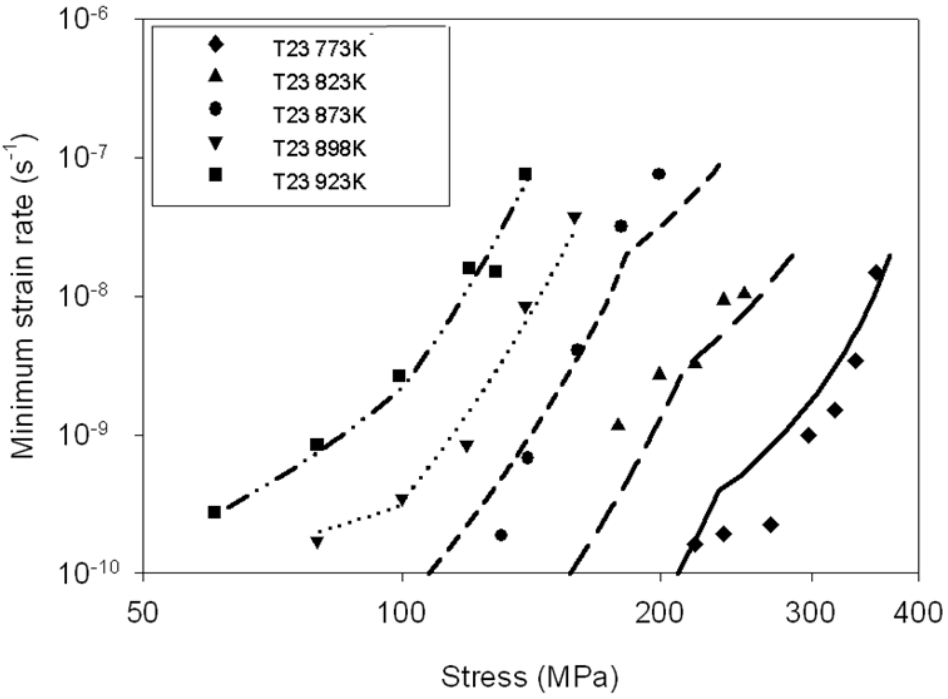

Fig 7. The stress dependence of the minimum creep rate at 773 to 923K for 2.25Cr-1.6W steel tube (T23). The lines are drawn after analysing the results according to Eq. (4).

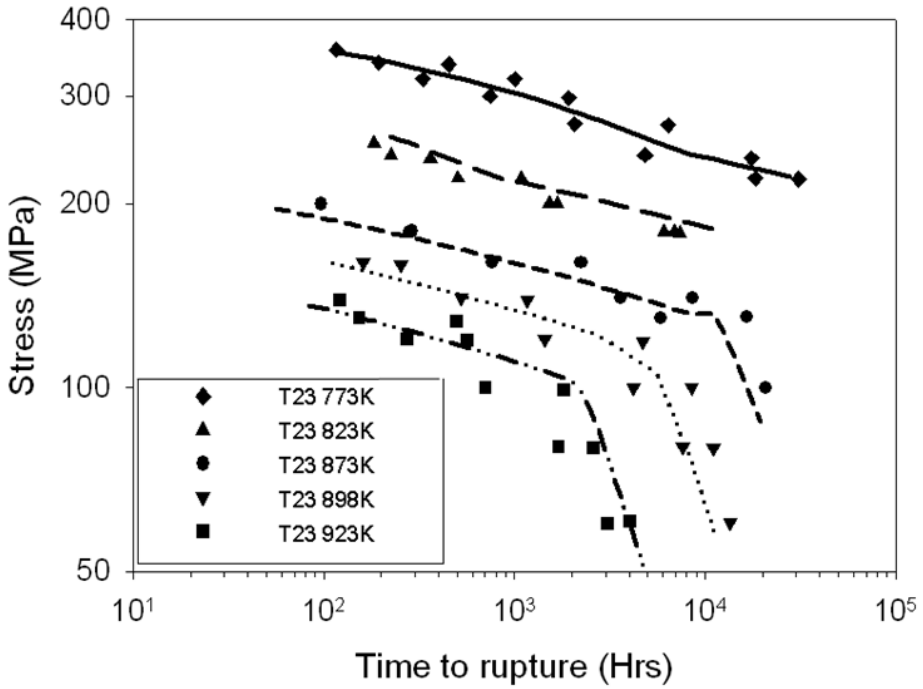

Fig 8. The stress dependence of the creep life at 773 to 923K for 2.25Cr-1.6W steel tube (T23). The lines are drawn after analysing the results according to Eq. (3).

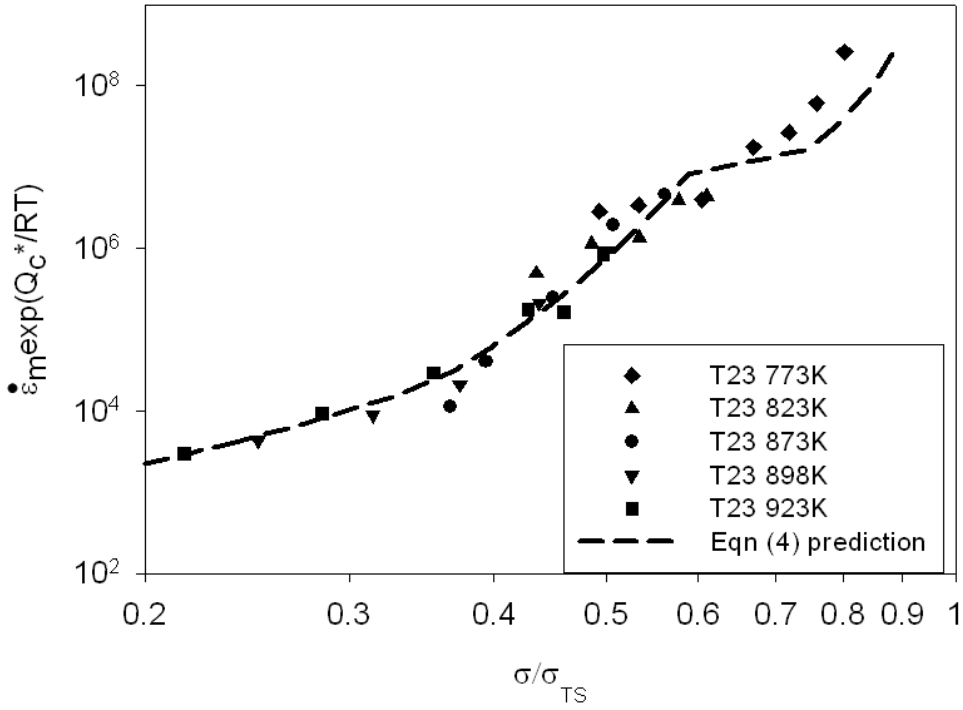

Fig 9. The dependence of log($\dot{\varepsilon}_m$ .exp 230,000/RT) on log (σ/σ_{TS}) at 773 to 923K for 2.25Cr-1.6W steel tube (T23) with the predicted line obtained using Eq. (4).

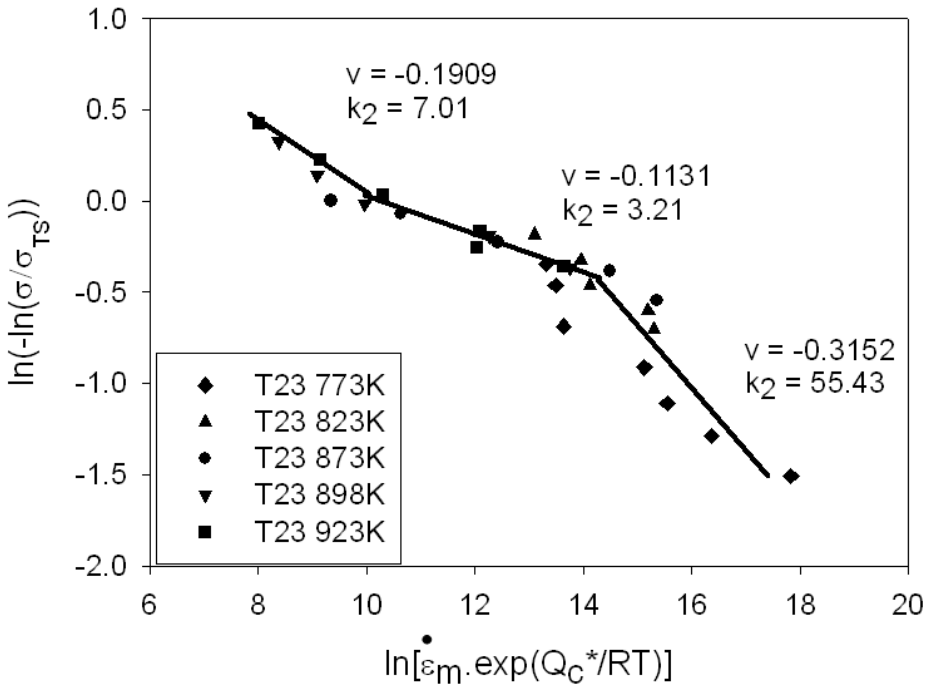

Fig 11. The dependence of ln($\dot{\varepsilon}_m$.exp 230,000/RT) on ln(-ln(σ/σ_{TS})) at 773 to 923K for 2.25Cr-1.6W steel tube (T23) using Eq. (4).

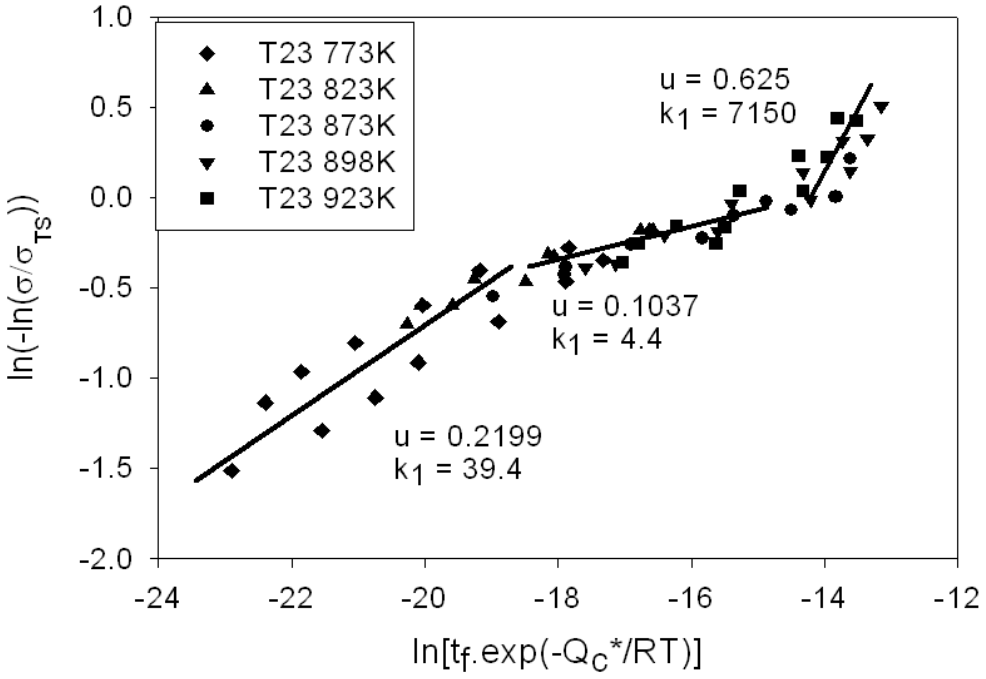

Fig 12. The dependence of $\ln(t_f.\exp -230{,}000/RT)$ on $\ln(-\ln(\sigma/\sigma_{TS}))$ at 773 to 923K for 2.25Cr-1.6W steel tube (T23) using Eq. (3).

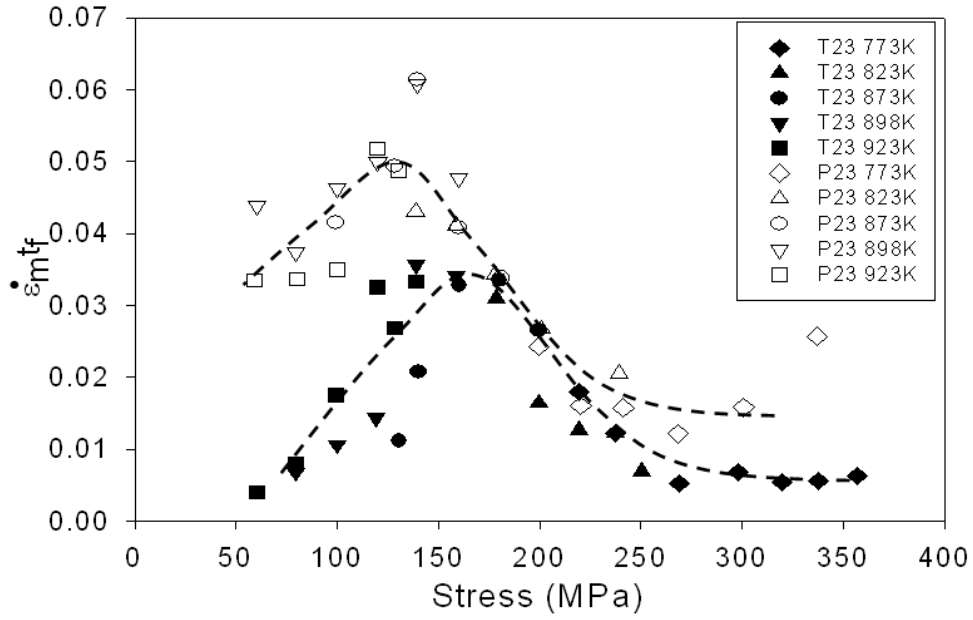

Fig 13. The stress dependence of $\dot{\varepsilon}_m t_f$ at 773 to 923K for 2.25Cr-1.6W steel pipe (P23) and tube (T23).

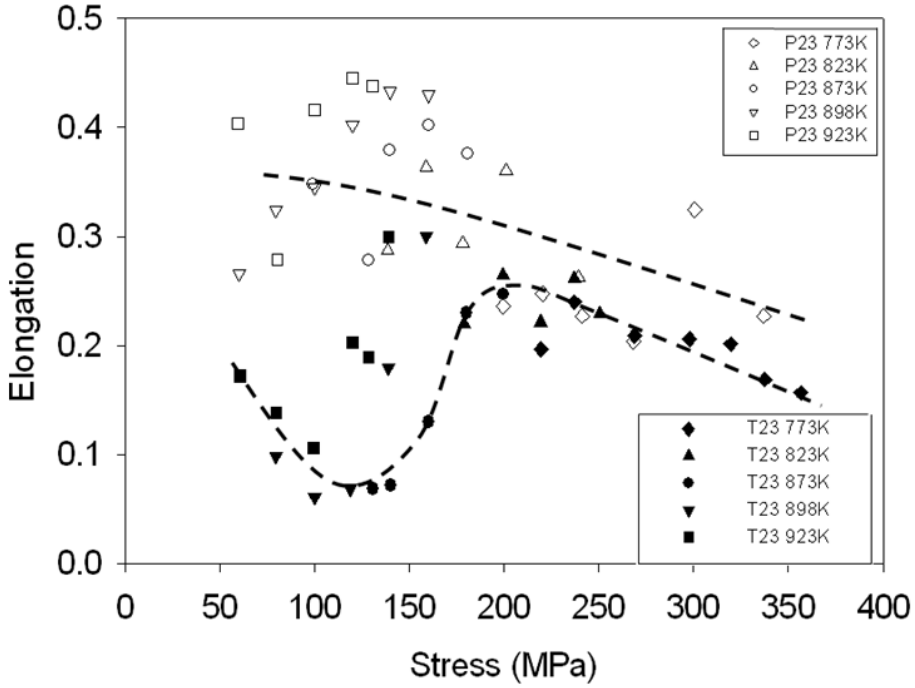

Fig 14. The stress dependence of the total strain to failure (ε_f) at 773 to 923K for 2.25Cr-1.6W steel pipe (P23) and tube (T23).

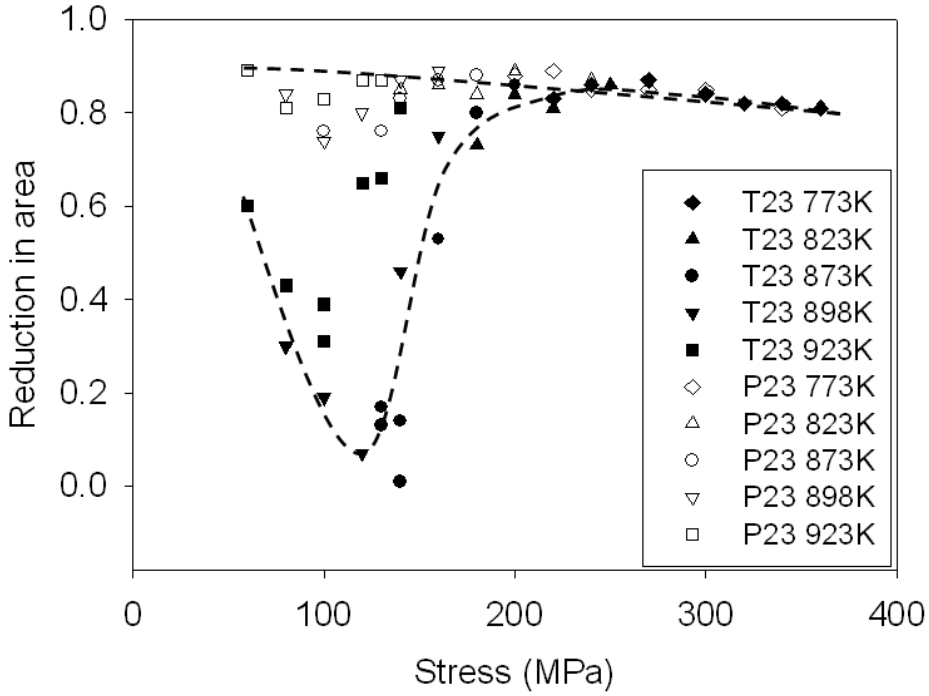

Fig 15. The stress dependence of the reduction in area at fracture (RoA) at 773 to 923K for 2.25Cr-1.6W steel pipe (P23) and tube (T23).

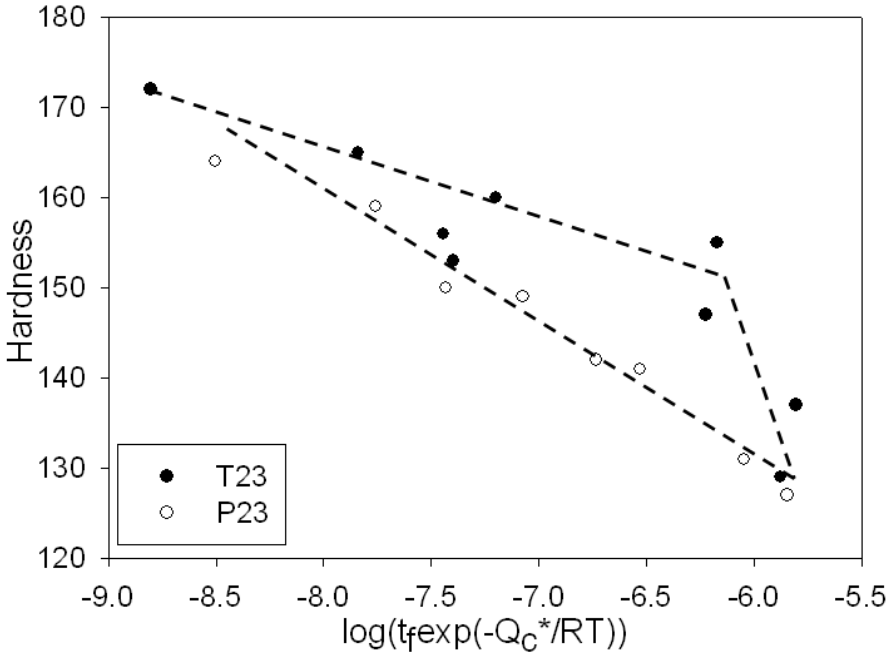

Fig 16. The dependence of the hardness (VDP) on log(t_f .exp -230,000/RT) at 773 to 923K for 2.25Cr-1.6W steel pipe (P23) and tube (T23).

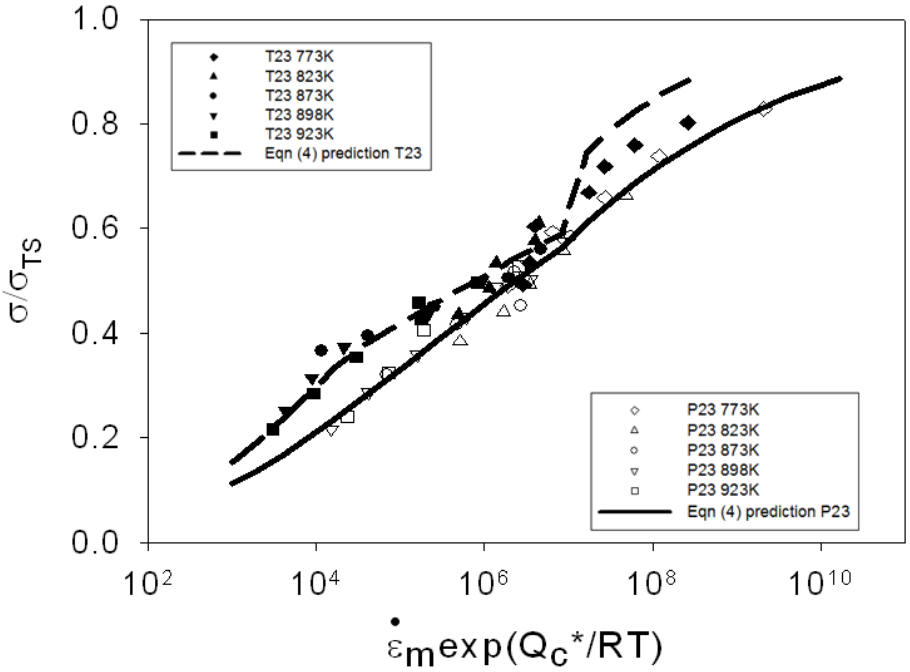

Fig 17. The dependence of log($\dot{\varepsilon}_m$ exp 230,000/RT) on (σ/σ_{TS}) at 773 to 923K for 2.25Cr-1.6W steel pipe (open symbols) and tube (closed symbols). The lines are predicted by data analysis using Eq. (4).

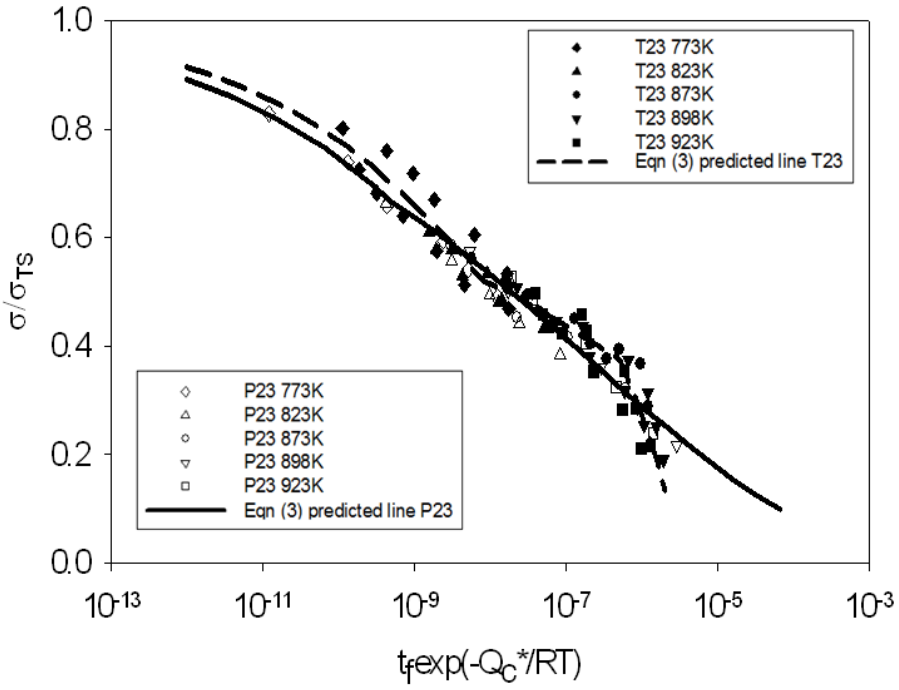

Fig 18. The dependence of log(t_f .exp -230,000/RT) on (σ/σ_{TS}) at 773 to 923K for 2.25Cr-1.6W steel pipe (open symbols) and tube (closed symbols). The lines are predicted by data analysis using Eq. (3).